

## Particles dispersion due to human prostration cycle and ventilation system in a prayer room



Douaa Al Assaad, Kamel Ghali, Nesreen Ghaddar\*

Mechanical Engineering Department, American University of Beirut, P.O. Box 11-0236, Beirut, 1107-2020, Lebanon

### ARTICLE INFO

#### Keywords:

Particle dispersion  
Indoor air quality  
Dynamic mesh  
Human prayer cycle  
Wake flow associated with prostration

### ABSTRACT

The aim of this study is to investigate the human wake flow field generated by prostration cycle during prayers and its impact on resuspended particles' dispersion. Prostration constituted of forward and backward rotations at 0.9 rad/s of the upper body towards and away from the floor respectively. The cycle was simulated by computational fluid dynamic (CFD) model that was coupled to a dynamic mesh to adapt to the moving manikin at a time step of 0.0005 s. The flow field was validated experimentally using a moving thermal manikin in a climatic chamber. The validated CFD model was used to track the dispersion of floor-resuspended particles using the Lagrangian technique at particle sizes of 1  $\mu\text{m}$  and 10  $\mu\text{m}$ .

It was shown the human prostration cycle disturbed the flow field in the person's microenvironment. The forward and backward rotations resulted in significant pressure gradients and a wake flow trailing behind the human body with peak velocities and turbulence intensities reaching 1 m/s and 20% respectively. During the backward rotation away from the floor, the flow was moving vertically upwards and was pushed out and pulled back into the wake. This behavior was the cause of the transport and dispersion of particles from the floor to higher levels in the space. Concentration fields showed that the breathable air quality was highly compromised near the floor. Moreover, 1  $\mu\text{m}$  particles presented a higher contamination risk than 10  $\mu\text{m}$  since they were transported more easily by the wake flow to the person's breathing zone.

### 1. Introduction

The indoor air quality (IAQ) of different spaces in the building sector has been investigated extensively in literature, as it is directly related to occupant health and wellbeing [1–3]. Air quality inside buildings is associated with the presence of passive contaminants and more critically active particulate matter [4]. Active contaminants originate from frequent human occupancy (coughing, sneezing, skin shedding) and particle carryover from the outside environment [5,6]. Indoor active particles can be airborne and directly infect occupants through inhalation causing several respiratory illnesses such as asthma [7] or other diseases such as eye irritations [8]. However, a large portion of these particles settle on indoor surfaces (floors, furniture ...) due to gravity and are added to the particles carried over from outside via walking. Therefore, over time, indoor surfaces become sinks or reservoirs for deposited particles.

Consequently, surfaces with large areas such as floors constitute a critical source of contamination through the possibility of particle resuspension. Particles detach from the floor if the adhesive forces are overcome by removal forces (mechanical, vibration, centrifugal) [9].

This detachment can occur in many modes which include particle rolling, sliding and lift off [10,11]. After being resuspended and depending on the flow field near the floor, they may get re-dispersed in the room bulk flow to reach and contaminate the occupant's breathing zone (BZ). Particle dispersion due to indoor human activities and its effect on the breathable air quality were investigated both numerically and experimentally in previous studies. Hyttiäinen et al. [12] studied experimentally particle dispersion after resuspension from carpeted bedroom floors due to a crawling toddler. They reported that the particles' concentration in the toddler's breathing level was 8–21 times higher than that of a standing adult. Using computational fluid dynamics (CFD), Tao et al. [13] investigated the effect of human walking speed on resuspended particles' transport from the floor. They reported that the swinging motion of the legs dispersed particles towards the upper body segments, especially during slow gait speeds.

However to the authors' knowledge, the impact of praying activity typically conducted in multi-faith spaces on particle dispersion has not been reported in literature. Multi-faith prayer rooms are small spaces frequented by occupants of different religious backgrounds to perform prayers. In some religions such as Islam, the praying person performs

\* Corresponding author.

E-mail address: [farah@aub.edu.lb](mailto:farah@aub.edu.lb) (N. Ghaddar).

<https://doi.org/10.1016/j.buildenv.2019.01.005>

Received 17 November 2018; Received in revised form 4 January 2019; Accepted 5 January 2019

Available online 07 January 2019

0360-1323/ © 2019 Elsevier Ltd. All rights reserved.

### Nomenclature

|            |   |
|------------|---|
| AHU        | Air handling unit                       |
| BZ         | Breathing zone                          |
| CFD        | Computational fluid dynamics            |
| DNS        | Direct numerical simulation             |
| DPM        | Discrete phase model                    |
| $d_p$      | Particle diameters in ( $\mu\text{m}$ ) |
| DRW        | Discrete random walk                    |
| $\Delta t$ | Time step size in (s)                   |

|           |  |
|-----------|--|
| IAQ       | Indoor air quality                       |
| $IF_{BZ}$ | Intake fraction at the BZ                |
| HVAC      | Heating ventilation and air conditioning |
| LES       | Large eddy simulations                   |
| MV        | Mixing ventilation                       |
| PIV       | Particle image velocimetry               |
| RANS      | Reynolds averaged Navier-Stokes          |
| $t$       | Time (s)                                 |
| UDF       | User defined function                    |

'prostration' starting off with a standing position and kneels towards the ground. This brings the person closer to the floor which constitutes a sink for active particles. After that, the praying person transitions between a kneeling posture and the 'prostration' position where the forehead and hands, come into contact with the floor. The impact of the forehead and hands on the floor is similar to the contact of the foot with the ground during walking. Thus, it may give rise to particle resuspension from the floor in prayer rooms. The resuspended particles can be directly inhaled by the praying occupant during prostration where the breathing zone (BZ) is very close to the ground. Moreover, the wake flow field generated by the rotation of the human body, combined with the background ventilation flow, can disperse the resuspended particles in the upper room levels. Therefore, particles can reach the occupant BZ as the occupant transitions back to the kneeling position which presents a health risk to the praying person.

The aim of this work is to study the dispersion of floor emitted particles due to occupant praying motion in a prayer room conditioned by a conventional mixing ventilation (MV) system. Additionally, the breathable air quality due to this dispersion is assessed. Particle resuspension from the floor is estimated by considering this surface as a source of pollution emitting particles. Moreover, the dynamic flow field generated by the prayer motion is modeled to study its effect on the particles' spreading for different particle sizes. To achieve this, a transient 3-D CFD model is developed for this study to predict the different airflow field variables (MV and human wake airflow fields) as well as particles' concentration and behavior. The CFD model is coupled with dynamic meshing modelling to simulate the praying motion of the thermal manikin and to accurately predict the induced wake flow field [13,14]. The flow field predictions by the CFD model with dynamic mesh are validated experimentally in a climatic chamber equipped with a MV system and moving thermal manikin.

## 2. Methodology

### 2.1. System and prostration cycle description

This study considers a multi-faith space conditioned by a conventional heating ventilation and air conditioning (HVAC) system which is the MV system [15,16]. MV systems supply cool fresh air from high levels in the space, either from a ceiling diffuser. The supplied air mixes with the warm polluted indoor, cools the space and dilutes contaminants. Therefore, MV system assures well mixed conditions in the space, with uniform temperature and concentration of pollutants [17,18]. In this work, the MV system is illustrated in Fig. 1(a) which presents the multi-faith room and the praying person. The MV system has the supply and exhaust diffusers at the ceiling level. Its air handling unit (AHU) supplies cool recirculated air into the room to provide an acceptable thermal environment for the praying occupants.

Islamic prayers involve many steps where the person starts off in a standing position and then transitions to a kneeling position. Note that the duration of each prayer step differs from person to person depending on age differences. In this study, typical durations were recorded by observing an average praying person of typical height of

1.7 m [19]. When the person is kneeling, the first step in the prayer prostration cycle would be for the upper body segments (back, abdomen, chest, arms, hands and head) to rotate forward around the hip segment. This rotation occurs at an average velocity of 0.9 rad/s at a radius of 1 m (0.82 m/s) [20]. The body rotates until the palms of the hands and the forehead come into contact with the floor and strike it. The rotation motion takes an average of 2 s to finish. This corresponds to Position 2 as seen in Fig. 1(b) which shows the different steps of the prayer cycle during prostration phase. In prayer, Position 2 of the body (hands and forehead in contact with the floor) is defined as "prostration" and the praying occupant remains in this position for approximately 4 s. After prostration, the upper body segments rotate in the opposite direction with the same speed, until they reach the initial kneeling position again and stop (Position 3 in Fig. 1(b)) for 4 s. Due to the rotation motion, the occupant's breathing zone (BZ) does not have a fixed location and varies between a low (prostration position) and a high (kneeling position). The BZ is defined as a sphere of diameter 2 cm situated at 2.5 cm away from the occupant's nose [21,22].

While standing, the person's BZ is far off from the contaminated

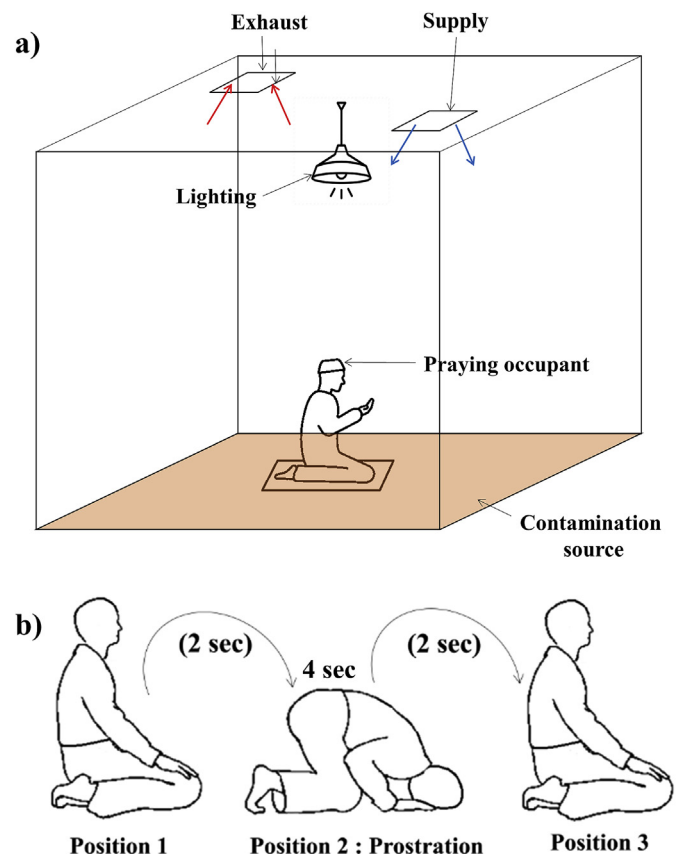


Fig. 1. Illustration of a) the praying room space conditioned by the MV system and occupied by the praying person, b) the different steps of the praying cycle.

floor. Additionally, the occupant remains still during the standing position and does not disturb the particles on the floor. When transitioning to a kneeling position, the occupant is closer to the polluted ground surface. Moreover, when the person performs prostration, the flow field in the occupant microenvironment is disturbed. Therefore, the prayer cycle of the current study is not considered in its entirety. The work is focused on a part of the prayer cycle named “prostration cycle” which is repeated twice and the critical kneeling posture is considered as the initial position (See Fig. 1(b)). Hence, the term “prostration cycle” in this work is used interchangeably with the “prayer cycle” term. The duration of the prayer cycle under consideration starting from the kneeling position lasts for an average duration of 12 s.

2.2. CFD modeling

In this study, the dynamic flow field in the room involves complex physical behaviors. This is due to the presence of the MV system which establishes a flow field characterized by significant turbulence intensities, as well as stagnant recirculation zones. On the other hand, the occupant is a heat source having a higher temperature than its ambient surrounding. Therefore, density differences generate thermal plumes which rise to the upper levels in the space. When the praying person starts to rotate, pressure differences will be established between the front and the back of the body forcing air movement. Consequently, a complex flow is generated due to the human wake flow that trails behind the body as well as the thermal plume. In addition, particles are emitted from the floor due to prostration. The particles are characterized by complex transient trajectories that depend on the MV flow field as well as the human wake flow. Consequently, in order to solve for the different flow field variables (velocity, temperature, particles' concentration ...), 3-D CFD modeling was adopted. The CFD model was used to understand the flow field behavior generated by the HVAC system and the human body motion. It was also used to track the discrete phase in the continuous phase and calculate their concentrations at different locations in the space.

Since 3-D CFD modeling was adopted, the commercial software ANSYS Fluent version 17.2 [23] was used to solve for the continuity, energy, pressure velocity coupling equations as well turbulent kinetic energy and dissipation rates equations. In order to represent the praying person in the CFD model, a computational thermal manikin model was used. The computational domain of the space with its different components as well as the thermal manikin with its different dimensions can be seen in Fig. 2.

2.2.1. Dynamic mesh model

To obtain accurate physical results for the flow field variables, the space needs to be accurately meshed. Due to the presence of a rotating thermal manikin in the space, the mesh needs to adapt itself to this motion while still preserving grid quality. Therefore, the mesh adopted in this study was a dynamic mesh. Dynamic meshing has been widely used in many studies to predict the behavior of flow fields in the presence of a time-dependent moving object and yielded good results [24–26]. When the manikin rotates forward and backward, a specific control volume in the space, encompassing the circular path followed by the manikin, is directly affected by the rotation motion while the rest of the space remains static. Therefore the mesh in the domain is divided into two zones: a static mesh zone and a dynamic mesh zone as can be seen in Fig. 3(a) and (b). The dynamic mesh zone and static mesh zones exchange information through their common interfaces, by applying the sliding mesh theory [23]. Therefore, instead of updating the mesh in the entire computational domain and risking the deterioration of the entire grid quality, only the dynamic mesh zone is affected. This meshing technique saves considerable computational time and preserves the mesh quality. Note that the spring based smoothing method as well as the local re-meshing methods have been applied to update the

mesh in the dynamic mesh zone [24] (See Fig. 3(b)). Due to the motion and the use of dynamic mesh, the developed CFD model is transient and should be advanced in time at a time step  $\Delta t$ . The choice of the time step should ensure that the distance crossed by the manikin is not too large that it causes the mesh elements to overlap causing negative cell volumes. For this study, several time steps were tested starting from  $\Delta t = 0.01$  s and decreasing it gradually. A time step of 0.0005 s was found adequate to update the mesh for the transient CFD model, while capturing the motion of the manikin during the prostration cycle.

For both static and dynamic mesh zones, an unstructured grid with tetrahedral elements was chosen. Face sizing of 1.5 cm, 2 cm and 6 cm were set for the manikin/floor, supply/exhaust and wall boundaries respectively. This grid configuration ensured a mesh independent solution with a maximum relative error of less than 5% [27]. Note that the relative error was defined based on the difference of average temperature in the  $y = 1.7$  m between two consecutive mesh configurations. The static mesh of the space was characterized by 352,646 elements and 65,476 nodes while the dynamic mesh zone is characterized by 169,678 elements and 32,897 nodes as can be seen in Fig. 3(b). The different mesh cases can be seen in Table 1.

2.2.2. Airflow modeling

The flow field mechanisms generated by the rotating thermal manikin and the MV system lead to high turbulence intensities in the space. Therefore, a proper turbulence model should be adopted. The application of direct numerical simulation (DNS) or large eddy simulations (LES) requires considerable computational cost and time especially with the use of dynamic mesh adopted in this work [25]. Consequently, the Reynolds-averaged Navier-Stokes (RANS) method was

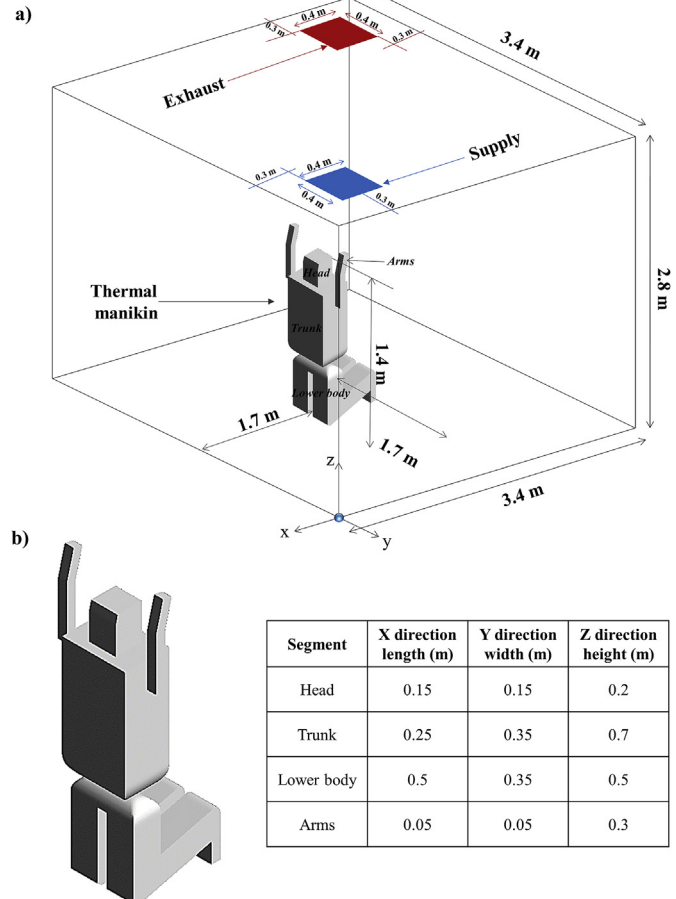


Fig. 2. Illustration of the computational domain equipped with the MV system and containing the manikin in its initial kneeling position.

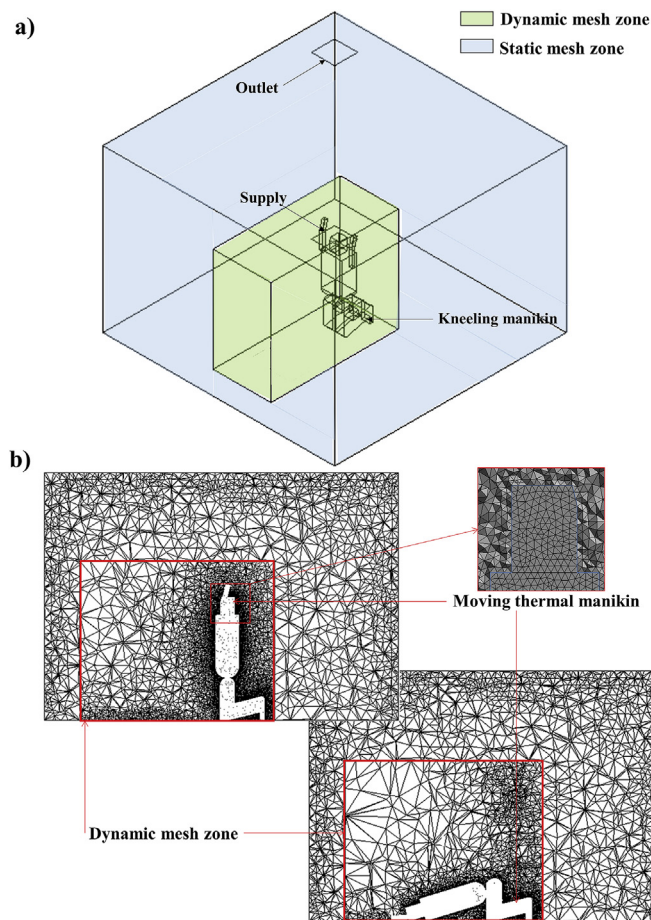


Fig. 3. Illustration of: a) the computational domain with the different mesh zones, b) the corresponding mesh during the kneeling and prostrating positions.

Table 1

Grid independence test using 5 different mesh cases.

|        | Face sizing<br>Manikin/walls<br>(cm) | Number of elements in<br>static (dynamic) zones | Relative error between two<br>consecutive meshes (%) |
|--------|--------------------------------------|---|--|
| Mesh 1 | 2/10                                 | 116,992 (113,118)                               | –  |
| Mesh 2 | 2/8                                  | 152,090 (113,118)                               | 34.1%  |
| Mesh 3 | 1.5/7                                | 183,708 (169,678)                               | 15.6%  |
| Mesh 4 | 1.5/6.5                              | 220,450 (169,678)                               | 6.3%   |
| Mesh 5 | 1.5/6                                | 352,646 (169,678)                               | 4.2%   |

chosen to model the unsteady flow and disturbances due to the moving occupant [28,29]. The RNG  $k-\epsilon$  model with enhanced wall treatment, was used due to its simplicity, robustness and accuracy in predicting airflow fields over solid bodies [30–32]. This model was adopted in the study of Tao et al. [13] on dynamic meshing modelling of human motion, and compared with other turbulence models. It was found that the RNG  $k-\epsilon$  model gave the most compatible results with experimental particle image velocimetry (PIV) measurements.

Since small density variations are present in the space, the Boussinesq approximation was chosen to account for buoyancy driven flows [24,33,34]. The momentum, energy,  $k$ ,  $\epsilon$  equations were discretized using the second order upwind scheme. As for pressure, the “PRESTO!” scheme was used since it accounts for pressure gradients at the boundaries [34]. In this study, human motion is considered; hence all variables are time dependent. As for the pressure-velocity coupling, the “PISO” algorithm was chosen due to its suitability in transient applications [23]. In order to consider a converged solution, several

criteria were taken into consideration. In fact, the scaled residuals were lower than  $10^{-8}$  for the energy equation and lower than  $10^{-6}$  for the rest of the variables [27]. Moreover, the net heat flux was 1% less than the total heat gained and mass balance was ensured in the space [35,36].

### 2.2.3. Discrete phase modeling for particles' transport

When the manikin approaches the floor, the physics involved are similar to the motion of the foot as it approaches the ground [37,38]. Khalifa et al. [37] investigated the unsteady film jet and particle resuspension, due to a falling foot, modeled by a uniformly descending flat object. It was shown that as the distance between the object and the floor decreases, the air gap between them is squeezed which generates high velocity radial jets [37]. This shear flow was shown to detach particles from the surface at a distance of 2 cm from the foot boundaries; for a small descending foot velocity of 0.5 m/s. The manikin's forehead and palms having comparable surface areas to that of the foot, are approaching the floor (Position 2 in Fig. 1(b)) at a higher velocity of 0.82 m/s. In this work, the particles are considered to be resuspended from areas 3 cm outside the forehead and palms' boundaries. These particles were chosen as dust particles having a density of  $2.5 \text{ g/cm}^3$  that were reported to be resuspended from carpeted surfaces, commonly used in multi-faith rooms [39]. The areas from which particles resuspend can be seen in Fig. 4 which represents a section of the human upper body in the prostration position.

Note that the aim of this study is to investigate particle dispersion. Hence, the floor was considered to be seeded by a certain mass of particles, and a fraction of these particles detach upon prostration, and remain very close to the floor. Consequently, the levitated particles were injected from the assigned surface areas (See Fig. 4) at a small height above the floor. Accordingly, the flow field generated by the manikin's rotation to the initial kneeling position (Position 1 in Fig. 1(b)) can disperse the injected particles. Note that a similar approach was adopted in the CFD model of Tao et al. [13], on particle dispersion due to human walking. They considered an imaginary plane above the floor where particles were injected and studied their dispersion once the human started walking.

The resuspended particles from the floor are affected by several forces. These forces include gravity forces which depends on particle diameter and causes the particles to settle and deposit on different surfaces. Other forces include the drag forces induced by the flow field (shear velocities and turbulence intensities) and defined using the spherical drag law [40,41]. There are also secondary forces such as the thermophoretic forces, Brownian motion and Saffman lift forces. These forces are two orders of magnitude smaller than the gravity and drag forces and will not be taken into account in this work [42–45]. To track the resuspended particles in the CFD model and thus solve for the particles' concentration, the discrete phase model (DPM) in Fluent, was used [46–48]. At first the airflow field was converged with the manikin in the initial kneeling position and then the rotation motion was assigned in ANSYS Fluent [23]. Once the manikin reaches the prostration position (See Fig. 3(b)), the particles were introduced into the space and tracked in time using the Lagrangian technique with the discrete random walk (DRW) model. The Lagrangian technique treats the particles as discrete phase and tracks their trajectories in space by solving for the second law of Newton [34,49]. This technique was adopted in the study of Tao et al. [13] and yielded good results which is why it was adopted in this work as well.

**2.2.3.1. Properties of DPM injections.** In this work, the particles were injected at a height of  $10^{-4} \text{ m}$  above the floor, within the boundaries of the assigned surfaces (See Fig. 4), at zero velocity, using a DPM injection file. This technique was also adopted in the study of Tao et al. [13] and Goldatesh et al. [50] in their CFD study on particle resuspension due to human walking.

As for particle diameters, typical diameters are considered due to

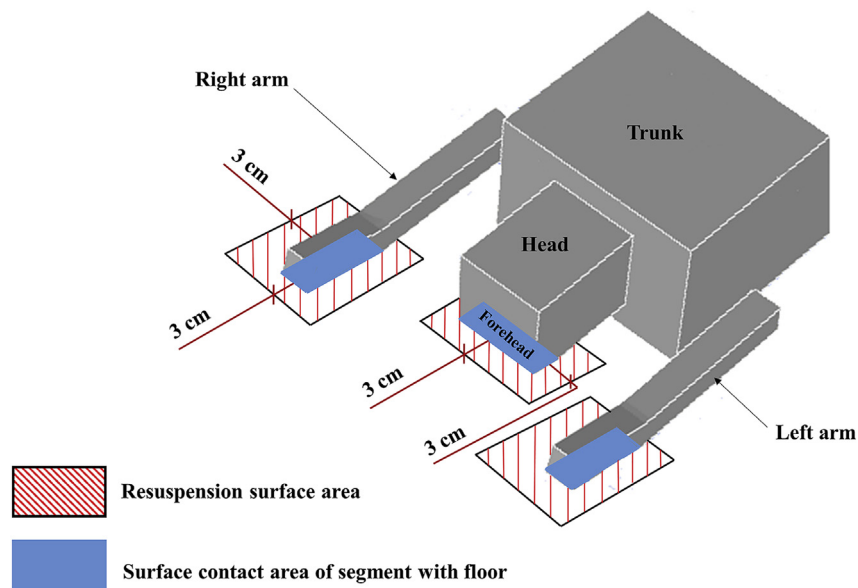


Fig. 4. Illustration of a cross section of the occupant upper body in the position of prostration with the different zones of particles' resuspension.

the varying position of the BZ. Therefore, two particle diameters of  $1\ \mu\text{m}$  and  $10\ \mu\text{m}$  were investigated in this work corresponding to the predominant resuspended particles in indoor spaces due to human activities [39]. The resuspension phenomena is considered to be instantaneous after the manikin impacts the floor at 2 s. Hence, these particles were injected instantaneously following the prostration at  $t = 2\ \text{s}$ . The fraction of detached particles was determined by analogy to the walking resuspension model of Goldasteh et al. [50]. In their study, the values of wall friction velocities due to foot impact were used to calculate the resuspended fraction of particles from the floor. By analogy, in this work, the prostration impact would resuspend 0.3% of seeded particles from the floor [50]. Consequently, for a typical dust loading of  $8.2\ \text{g}/\text{m}^2$  over a total surface area of  $0.2\ \text{m}^2$ , this corresponds to a resuspended particles' mass of 5 mg. Note that ANSYS Fluent tracks parcels representing a sample of particles having similar properties. In this work, 600,000 parcels were distributed uniformly across the injection surface areas for  $1\ \mu\text{m}$  and  $10\ \mu\text{m}$ . Note that the DPM method is a statistical approach, and the higher number of parcels, the better the convergence. In other words, the number of parcels should be enough to produce a statistical sample representative of the full range of particle behavior [23]. In this work, several simulations were performed with an increasing number of parcels and the fluctuations in the mean values of particle concentrations were estimated. It was found that a parcel number of 600,000 was enough to produce a convergent statistical sample with fluctuations smaller than 5% and a compromise between computational cost and accuracy [23]. In consequence, a total of 5 mg were injected instantaneously at  $10^{-4}\ \text{m}$  above the three surfaces, at  $t = 2\ \text{s}$  (See Fig. 4).

#### 2.2.4. Boundary conditions

A physical solution to the problem is determined by the proper assignment of the boundary conditions in the space. The MV supply diffuser is set as a velocity inlet having a constant velocity, specified air-flow temperature, turbulence intensity and length scale. The MV exhaust diffuser is assigned as a pressure outlet with zero gauge pressure, turbulence intensity and hydraulic diameter. Surfaces such as walls, floor, ceiling, and thermal manikin are assigned as walls generating a heat flux adding to the room load to be removed by the MV system. Note that to model the manikin rotation motion, a user defined function (UDF) was assigned as a condition in the dynamic mesh settings. The boundary conditions used in the CFD model of the different surfaces are summarized in Table 2(a).

As for the boundary conditions related to the DPM model for particles' tracking, the exhaust was assigned as an escape condition. This means that the DPM model stops tracking the particles when they have exited the space. Wall boundaries (thermal manikin, floor, walls, ceiling) are assigned as a trap condition, which means that particles reaching these boundaries have deposited on the assigned surfaces. As for other particles, they remain tracked by the DPM model in the space.

#### 2.3. Occupant contamination assessment

Upon dispersion, particles of diameter  $1\ \mu\text{m}$  or  $10\ \mu\text{m}$  [39] can reach the occupant BZ and be directly inhaled. Since the person is moving, the BZ location and the breathable air quality vary with the angular position of the occupant with respect to the vertical  $z$ -axis. Hence, it is important to assess contamination with time at the BZ when the occupant changes position. It is noteworthy that some BZ positions are more critical than others such as during prostration since the occupant is close to the source of contamination for a long period of time (4 s). In order to assess the risk of direct contamination during the prayer cycle (See Fig. 1(b)), the time-dependent intake fraction  $IF_{BZ}$  used in previous studies [34], is defined in equation (1) below:

$$IF_{BZ} = \frac{\text{Particles' concentration at the BZ of the occupant}}{\text{Concentration of particles detached from floor surface}} \quad (1)$$

This index represents the percentage of particles inhaled from the breathing zone at any time during the prostration cycle by the praying person from a polluting source which is the floor in this case. Hence at each BZ time-dependent position, the  $IF_{BZ}$  is averaged in space over the BZ surface area and evaluated for particle diameters of  $1\ \mu\text{m}$  and  $10\ \mu\text{m}$ .

#### 2.4. Experimental methodology

The developed CFD model presented above predicted the flow field behavior in the space, which was used as input by the DPM model in ANSYS Fluent [23]. In addition, the dynamic mesh adopted in this study predicted the velocity fields in the space due to the manikin forward and backward rotational motions. Therefore, accurate numerical values of velocity were needed for accurate prediction of particle behavior in the room and especially in the praying person surrounding. Consequently, experiments were conducted in a climatic chamber equipped with a MV system to ensure the validity of the CFD and dynamic mesh models in predicting time-dependent velocity fields in the

**Table 2**  
The different boundary conditions used in the CFD model and measured experimentally.

| a) Boundary conditions for the CFD configuration  |  |
|---|--|
| Boundary  | Condition  |
| MV supply   | Velocity inlet (constant value): 0.4 m/s<br>Constant inlet temperature: 19 °C<br>Turbulence intensity: 5%<br>Hydraulic diameter: 0.451 m<br>DPM condition: Reflect   |
| MV exhaust  | Pressure outlet, zero gauge pressure<br>Turbulence intensity: 5%<br>Hydraulic diameter: 0.451 m<br>DPM condition: Escape   |
| Thermal manikin upper body (head, arms and trunk) | Rotating Walls with constant heat flux (39 W/m <sup>2</sup> ) and a constant rotation speed of 0.9 rad/s<br>DPM condition: Trap  |
| Ceiling, walls, thermal manikin lower body        | Fixed walls with constant heat flux<br>Ceiling (10 W/m <sup>2</sup> )<br>Walls (10 W/m <sup>2</sup> )<br>Thermal manikin lower body (39 W/m <sup>2</sup> )<br>DPM condition: Trap  |
| Floor   | Fixed walls<br>DPM condition: Trap   |
| b) Boundary conditions measured experimentally    |  |
| MV supply   | Measured velocity: 0.4 ± 0.1 m/s (Inlet flow rate 64 L/s).<br>Measured inlet temperature: 19 ± 0.3 °C<br>Turbulence intensity: 5 ± 1%<br>Instrument used: OMEGA HHF2005HW model characterized by an accuracy of ± 0.5 °C for temperature and ± 10% of full scale velocity measurement, ranging between 0.2 m/s and 20 m/s.   |
| MV exhaust  | Exhaust flow rate: 64 L/s<br>Measured outlet temperature: 24 ± 0.3 °C<br>Turbulence intensity: 5 ± 1%<br>Instrument used: OMEGA HHF2005HW model characterized by an accuracy of ± 0.5 °C for temperature and ± 10% of full scale velocity measurement, ranging between 0.2 m/s and 20 m/s.   |
| Thermal manikin upper body (head, arms and trunk) | Surface heat flux due to 75 W heat source: 39 W/m <sup>2</sup><br>Rotation speed: 0.9 rad/s<br>Instruments used:<br>- CM series, 20CM003 model 2-phase Leadshine stepper motor, characterized by a 0.03 N m holding torque, and a 0.6 A phase current<br>- SWEMA03 anemometers having a temperature measurement accuracy of ± 0.1 °C and velocity measurements ranging between 0.05 m/s and 3 m/s with an accuracy of ± 4% and a response time of 0.2 s + real time data logging (SWEMA Multipoint software) |
| Ceiling, walls, thermal manikin lower body        | Ceiling lights (100 W)<br>Walls with U-value of 1.5 W/m <sup>2</sup> K (10 W/m <sup>2</sup> )<br>$\Delta T_{in-out}$ measured using OMEGA T-type thermocouples having a measurement accuracy of ± 0.1 °C and connected to an OMEGA data logger.<br>Thermal manikin lower body (39 W/m <sup>2</sup> )   |

space.

The experimental chamber is similar to the space used in the CFD model and shown in Figs. 2 and 5(a) with its various elements and dimensions. The different measured boundary conditions in the experimental chamber are presented in Table 2(b). The MV system supplied cool recirculated air at a velocity of 0.4 m/s and a temperature of 19 °C assuring a temperature of 24 °C inside the space. In the middle of the room, a thermal manikin representing a praying occupant in a prayer room, was positioned (See Fig. 5(b)). The thermal manikin was manufactured with 3 mm-thick aluminum sheets and had the same dimensions as the computational thermal manikin (See Fig. 2(b)) which mimicked the anatomy of an average 1.7 m tall human [51]. The manikin was divided into 2 parts: the moving upper body (head, hands,

trunk and arms) and the fixed lower body. Note that the different segments (head, hands, trunk and arms, lower body) were connected one with the other. The inside of the manikin was equipped with a heat source of 75 W identical to the heat flux generated by an occupant at sedentary activity or standing person. The heat source was placed in the middle of the manikin's body at a height of 0.7 m in order to insure a uniform heat flux distribution of 39 W/m<sup>2</sup> among the different segments. Note that the manikin edges were insulated with Styrofoam insulation having a U-value of 1.14 W/m<sup>2</sup>.K. The manikin upper body (see dimensions in Fig. 2(b)) was connected to a shaft which is coupled to a stepper motor; controlled using Arduino hardware and software. The stepper motor used was a CM series, 20CM003 model 2-phase Leadshine stepper motor, characterized by a 0.03 N m holding torque, and a 0.6 A phase current. The manikin performed the different steps of the prayer cycle defined previously and illustrated in Fig. 1(b). The velocities were measured with time as the manikin shifted from Position 1 to Position 2 in 2 s, as the manikin remained in Position 2 (4 s) and when the manikin shifted back to Position 2 in 2 s. To measure the angular velocity of the manikin, the time required for the manikin to reach the prostration was measured using a stop watch. Knowing the angle the manikin forms with the vertical z axis and the recorded time, the angular velocity can be calculated and used as input in the CFD model. All of the different boundary conditions measured experimentally and used later on as input into the CFD model are summarized in Table 2.

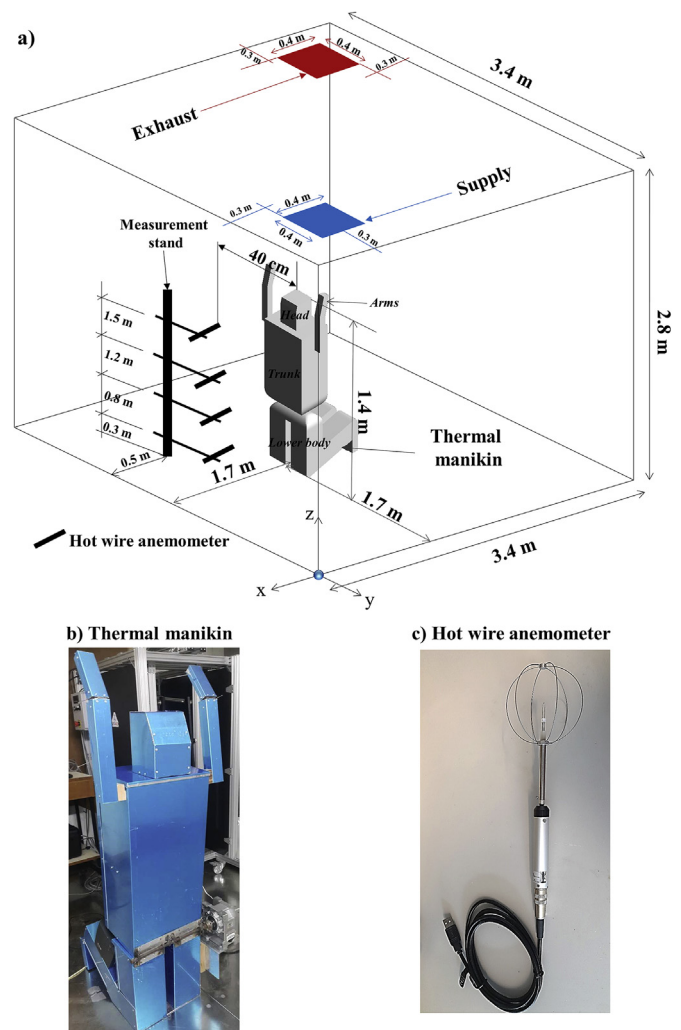


**Fig. 5.** Illustration of a) the experimental chamber equipped with a MV system, b) thermal manikin and c) SWEMA03 hot wire anemometer system.

To perform velocity measurements, omnidirectional hot wire anemometers were used (See Fig. 5(c)). The hot wires used to measure the velocities, temperatures and turbulence intensities of the MV supply and exhaust were OMEGA HHF2005HW models characterized by an accuracy of  $\pm 0.5\text{ }^{\circ}\text{C}$  for temperature and  $\pm 10\%$  of full scale velocity measurement, ranging between 0.2 m/s and 20 m/s. Another time of hot wires used were SWEMA03 anemometers having a temperature measurement accuracy of  $\pm 0.1\text{ }^{\circ}\text{C}$  and velocity measurements ranging between 0.05 m/s and 3 m/s with an accuracy of  $\pm 4\%$  and a response time of 0.2 s. The anemometers were equipped with SWEMA Multipoint software allowing for real time data logging of thermal and velocity fields. These hot wires were placed along the manikin's radial path at a y-distance of 40 cm from the manikin mid-plane ( $y = 1.7\text{ m}$ ) and x-distance of 0.5 m from the wall (See Fig. 5). The velocities were measured at 4 different heights (0.3 m, 0.8 m, 1.2 m and 1.5 m). Consequently, as the manikin rotated forward from Position 1 to Position 2, it disturbed the air in its vicinity. Hence, the hot wires could sense the motion and measure the corresponding airflow velocities as they were changing with time. When the manikin stopped moving in Position 2, the turbulence intensity in the air dropped and the hot wire could sense the decrease in velocities. Finally, as the manikin rotated backward to Position 2, the hot wires could sense the increase in velocities once more. Note that this technique was also adopted in previous studies of Han et al. to validate their CFD model's ability in predicting the wake flow field of a walking manikin.

#### 2.4.1. Experimental protocol

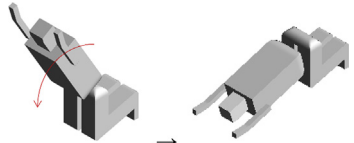
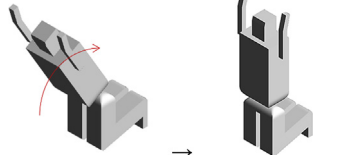
The experiment was initiated by turning on the MV system and the lights (100 W) inside the room. The thermal manikin heat source was then turned on and set to emit 75 W. The MV supply velocity and temperature were set at 0.4 m/s and  $19\text{ }^{\circ}\text{C}$  to remove a typical load of  $25\text{ W/m}^2$  due to manikin (75 W), lighting (100 W) and walls (100 W) assuring a room temperature of  $24\text{ }^{\circ}\text{C}$  (See Table 2). Note that the heat flux from the walls was measured using an OMEGA heat flux meter OS-652 model characterized by an accuracy of  $\pm 1\%$  for heat flux measurement at ambient temperature of  $-18\text{ }^{\circ}\text{C}$  to  $43\text{ }^{\circ}\text{C}$  and response time of 1 s. After 5 h of running the experiment, the flow field in the room reached steady state conditions. In fact, a total heat of 275 W was generated by the internal loads in the room (walls, manikin and lighting) and the inlet air was supplied at  $19\text{ }^{\circ}\text{C}$ . This caused the outlet air temperature to rise by  $3.5 \pm 0.3\text{ }^{\circ}\text{C}$ . Therefore, heat balance was ensured in the system. On the other hand, the measured supplied inlet and outlet flow rates were equal since there was no moisture generation in the room, and infiltration was minimal. Hence, mass balance was also ensured. Initially, the manikin was in the kneeling position of prayer (Position 1 as seen in Fig. 1(b)). The prayer cycle was initiated using the Arduino hardware and the manikin performed the same prayer cycle described previously. Subsequently, real time velocities were instantly measured at different heights, logged and then compared with CFD model results. Both experimental sets were repeated five times to ensure consistency of the results and accuracy.

### 3. Results and discussion

When the person performs forward and backward rotational motions in the space, the velocity and pressure fields in the vicinity are affected. In addition, the behavior of the wake flow dictates the behavior of particles near the occupant and thus the breathable air quality and risk of contamination. The experimental chamber was modeled numerically by CFD and the boundary conditions used as input in the model (MV supply, exhaust, thermal manikin ...) were measured experimentally (Table 2). At first, the CFD model results were obtained and presented in this section for the airflow field to understand its dynamic behavior and to validate the airflow velocity fields. Then, the DPM model was run to track the dispersion of resuspended particles' and assess the breathable air quality for particle diameters commonly

**Table 3**

Description and illustration of the different instances constituting the prayer cycle.

| Phase                   | Description   | Illustration  |
|-------------------------|---|---|
| Phase 1:<br>I1<br>(6 s) | The manikin rotates forward (2 s) towards the prostration position at the floor (4 s) |  |
| Phase 2:<br>I2<br>(6 s) | The manikin rotates backward (2 s) towards the kneeling position (4 s)                |  |

found indoors:  $1\text{ }\mu\text{m}$  and  $10\text{ }\mu\text{m}$ . A small particle diameter ( $1\text{ }\mu\text{m}$ ) and a larger one ( $10\text{ }\mu\text{m}$ ) were selected to study the effect of particle size on the breathable air quality.

#### 3.1. Airflow field behavior and validation

The prayer cycle previously described is divided into two phases. The first phase that starts at instant I1 includes the forward rotation (2 s) and the prostration (4 s) and the second phase that starts at instant I2 includes the backward rotation (2 s) to the initial kneeling position (4 s). The different phases can be seen in Table 3. These phases I1 and I2 are discussed below based on the airflow field direction, streamlines, velocity, pressure gradients and turbulence intensities.

Fig. 6 represents velocity contours and vectors, pressure contours in the  $y = 1.7\text{ m}$  mid-plane, as well as streamlines, between 0 s (before the motion) and 2 s (as the manikin reaches prostration). At time  $t = 0\text{ s}$ , it can be seen that buoyant thermal plumes moved upwards from the different segments of the thermal manikin at a velocity of 0.2 m/s and reached higher levels in the space. Moreover, the MV flow field established a quiescent environment with low background velocities ranging between 0.05 and 0.1 m/s as can be seen in Fig. 6 at time 0 s. Note that the initial turbulence intensities in the space reached maximum values of 10% and were found near the floor before the manikin started moving. Fig. 7 shows the turbulence intensities contours for the praying cycle starting from the kneeling position: [0 s–12 s]. It is clear that at  $t = 0\text{ s}$ , the turbulent intensity is highest near the floor. Moreover, no airflow was circulating around the fixed manikin body as seen from diminished pressure differences between the front and back of the manikin (see Fig. 6 at  $t = 0\text{ s}$ ). This is supported by the experimentally measured and predicted values of velocity provided in Fig. 8 which shows their variation with time during the prostration cycle at the 4 different heights ( $z = 0.3\text{ m}$ ,  $z = 0.8\text{ m}$ ,  $z = 1.2\text{ m}$ ,  $z = 1.5\text{ m}$ ). In addition, the predicted and measured background velocities at  $t = 0\text{ s}$  and at all heights were 0.065 m/s and  $0.07 \pm 0.02\text{ m/s}$  respectively. Furthermore, good agreement was obtained between experimental and predicted velocities with a maximum relative error of 7.14% at  $z = 0.3\text{ m}$ .

When the prayer cycle starts (phase I1), pressure difference ensued between the front and back sides of the manikin. High pressure region built up at the front of the body while a low pressure region was observed at the backline. This drove the airflow from the front to the back of the manikin body. This can be seen from the pressure contours in Fig. 6 at times 0.5 s, 1.5 s and 2 s. According to Fig. 6, a constant pressure difference of 1.6 Pa existed between the front and the back and was maintained before the manikin reached the prostration position at 2 s. This pressure difference did not vary since the rotation velocity of the manikin between 0 s and 2 s remained constant. The local airflow

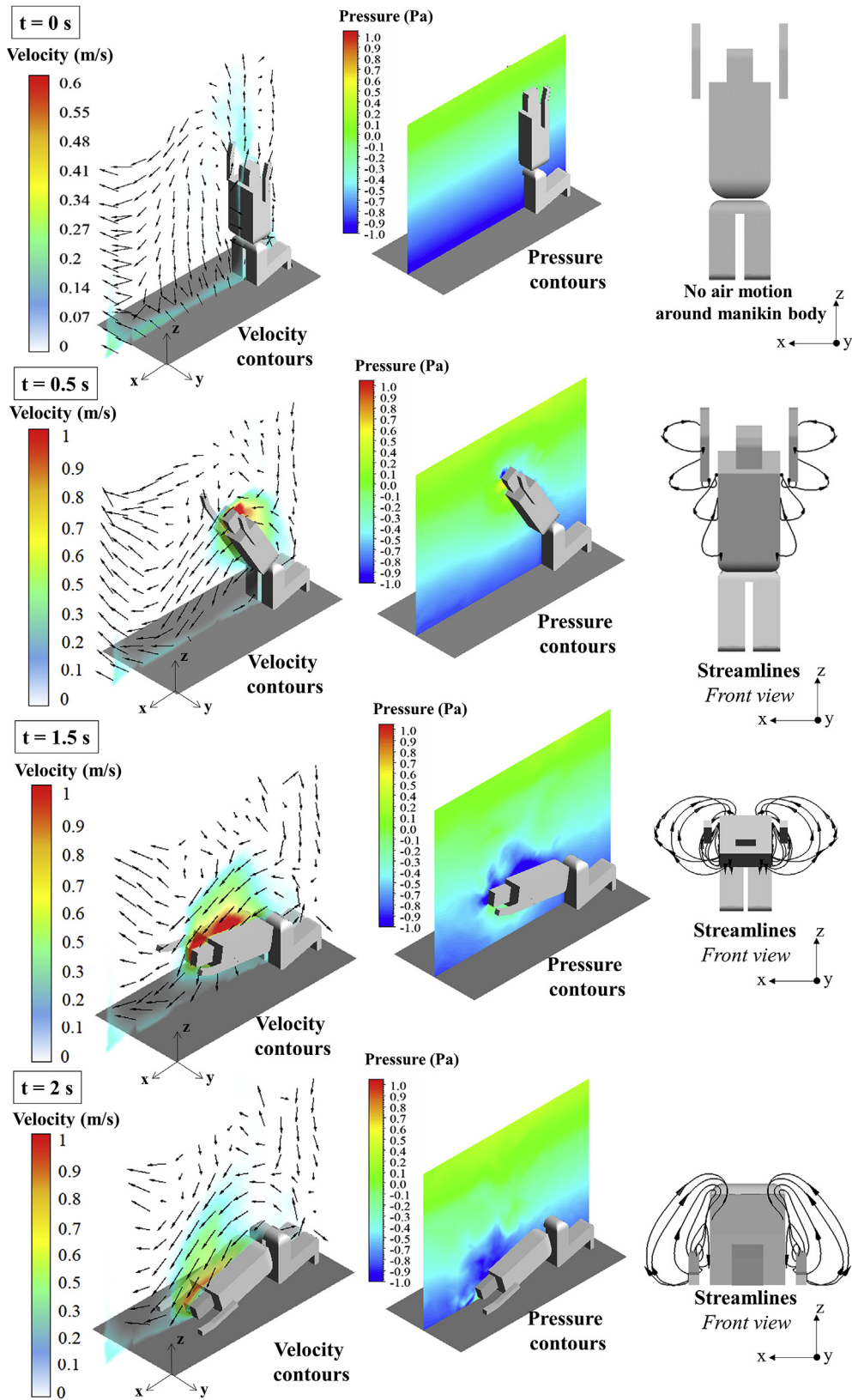


Fig. 6. Illustration of velocity contours, pressure contours in the y center plane ( $y = 1.7$  m) and 3-D velocity streamlines between  $t = [0\text{ s} - 2\text{ s}]$ .

behavior around the manikin body can be also seen in the streamlines shown in Fig. 6. At times 0.5 s, 1.5 s and 2 s, streamlines originated from the front, wrapped around and curled back into the manikin body. This shows that there was airflow entrainment induced by the rotating

manikin which pushed the air in front of it. The displaced air joined the flow at the back of the body to occupy the void left by the manikin. This airflow field behavior increased turbulence intensities to 20% behind the head and back of the manikin (see Fig. 7 [0.5 s–2 s]). Note that

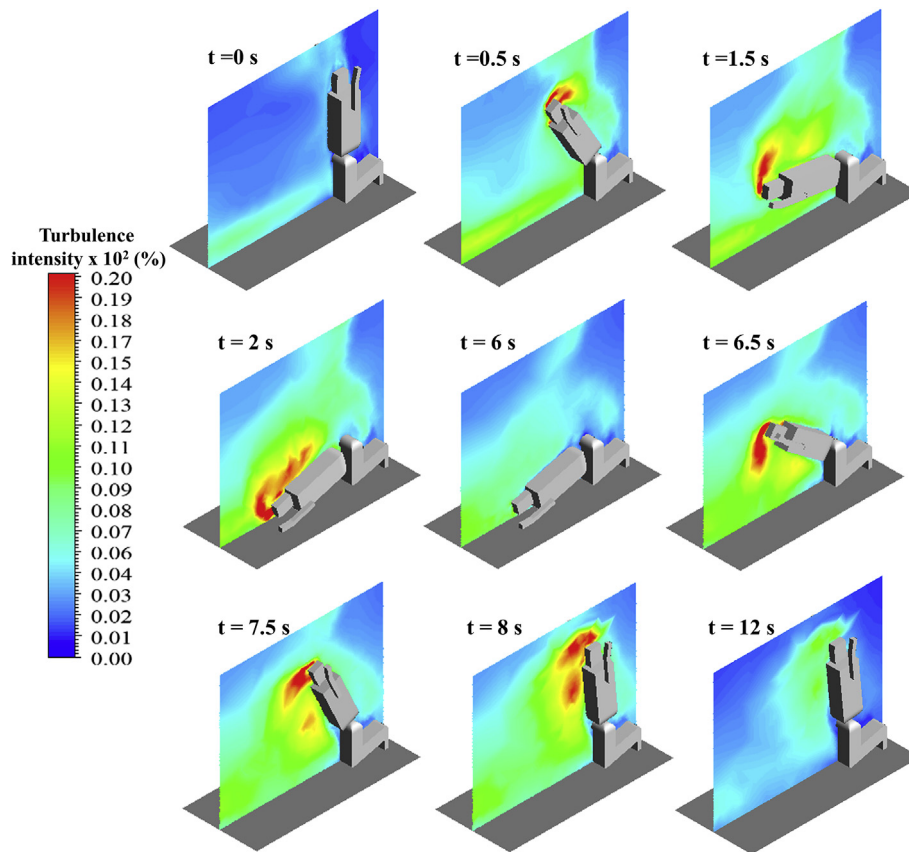


Fig. 7. Illustration of the contours of turbulence intensities (%) for the entire duration of the prayer cycle: [0 s–12 s].

during the forward rotation between 0 s and 2 s, the streamlines remained close to the body.

Due to the pressure driven airflow from the front to the back, a wake flow field region trailed behind the manikin body. The wake flow between 0 s and 2 s can be seen in the velocity contours and vectors at the  $y = 1.7$  m plane shown in Fig. 6, for a moving manikin speed of 0.82 m/s. According to Fig. 6, the wake had a triangular shape with peak velocities of 1 m/s found at the back of the head and upper trunk areas. Note that the initially rising thermal plume still persisted despite being disturbed by the motion. According to the velocity vectors between [0.5 s - 2 s] in Fig. 6, the region between the manikin's current and initial kneeling positions showed that the flow was moving downwards catching up to the manikin body. Additionally, as the motion progressed in time, the wake flow length increased since the manikin crosses a longer distance and more air was entrained into the wake. At the final prostration position at 2 s, the wake reached a maximum length of 1.4 m.

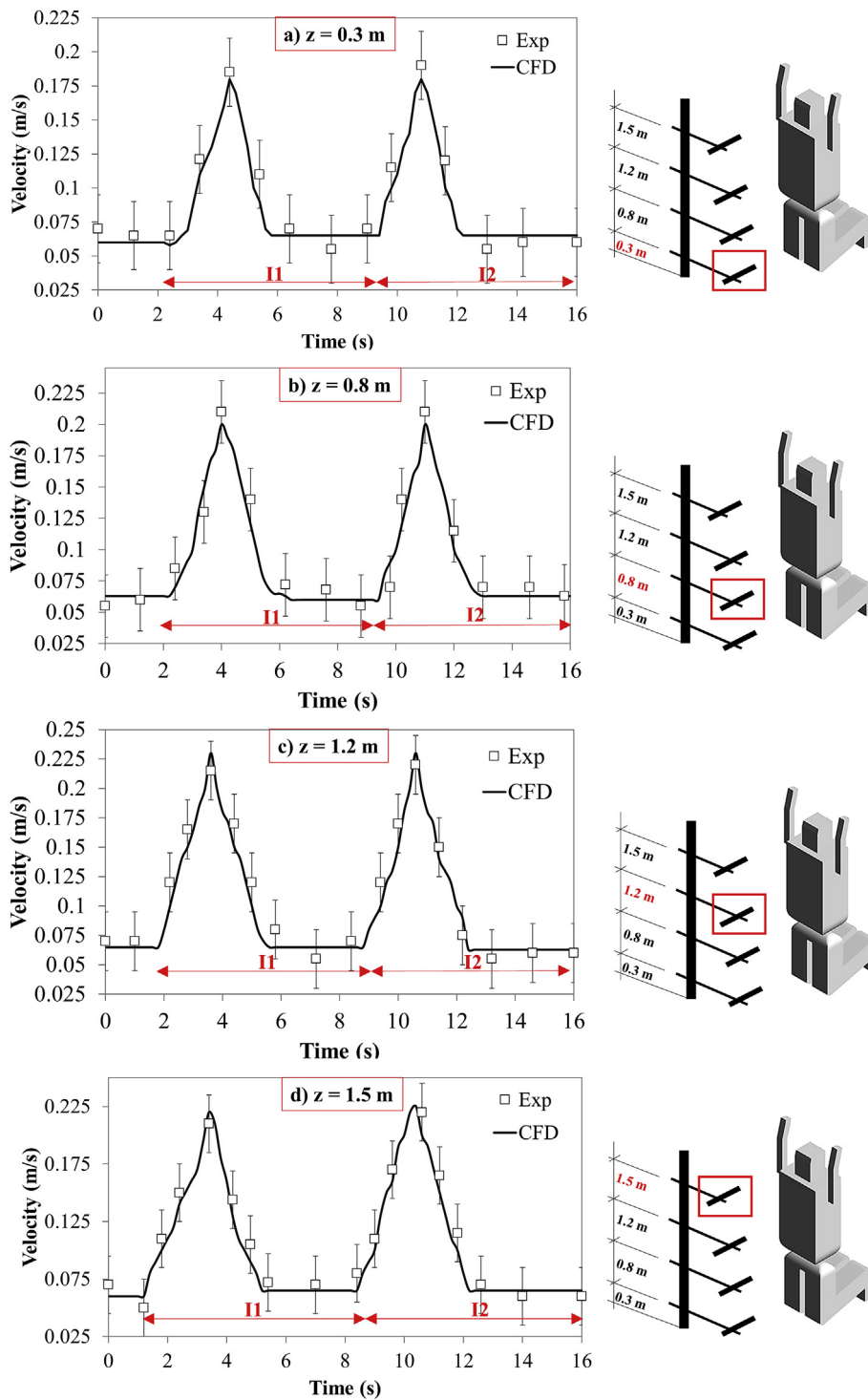
The manikin motion between 0 s and 2 s also disturbed the micro-environment surrounding the manikin. According to Fig. 8 during I1, the measured and predicted velocities increased gradually at the different heights as the manikin approached the measurement locations seen in Fig. 5(a). The predicted/measured velocities reach maximum values of 0.18 m/s ( $0.19 \pm 0.02$  m/s), 0.2 m/s ( $0.21 \pm 0.02$  m/s), 0.22 m/s ( $0.21 \pm 0.02$  m/s) and 0.22 m/s ( $0.21 \pm 0.02$  m/s) for heights of  $z = 0.3$  m, 0.8 m, 1.2 m and 1.5 m respectively. Good agreement was also found between experimental and predicted values with a maximum relative error of 13.3% obtained at  $z = 0.8$  m at 3.5 s. Smaller peak velocities were found at  $z = 0.3$  m since this height corresponds to the height of the fixed lower body which is the furthest from the wake flow field. At the higher levels ( $z = 0.8$  m, 1.2 m and 1.5 m), higher velocities were found since these measuring locations were closest to the turbulent wake flow field. It can also be seen in

Fig. 8 during I1 that after the manikin crossed the measuring locations, the velocities at all heights decreased after the peak, to reach the background velocities once more.

After the manikin reached the prostration position at 2 s, the manikin stayed still in the prostration position until  $t = 6$  s. Fig. 9 illustrates the velocity vectors and contours, pressure contours at the  $y = 1.7$  m mid-plane, as well as streamlines between 6 s and 12 s. According to Fig. 9 at  $t = 6$  s, it can be seen from the pressure contours and streamlines that there was no pressure difference or airflow circulation between the front and back. Moreover, turbulence intensities at the head and back dropped to 12% (see Fig. 7,  $t = 6$  s). As for the wake, its velocity diminished to 0.2 m/s and according to the velocity vectors; the wake was transported in front of the manikin (see Fig. 9 at  $t = 6$  s). Note that the thermal plume hasn't had the time to rise again from the body during the prostration position. According to Fig. 8 during I1, predicted and measured velocities at all heights dropped to the background velocities. This was due to the dissipation of the wake flow as well as the 40% decrease in turbulence intensities around the manikin.

At  $t = 6$  s, the motion reversed direction and the manikin rotated backward to the initial kneeling position at  $t = 8$  s (phase I2). The physics governing the airflow behavior in the backward rotation was similar to the forward rotation. The pressure difference (1.6 Pa) drove the airflow from the back to the front (see Fig. 9). Additionally, similar streamlines originated from the back, wrap around and curled back to the front of the manikin body. However, in this case, the streamlines moved further away from the body. Due to this airflow behavior, similar turbulence intensities of 20% were found at the front of the head (hence the BZ) and the upper trunk area (See Fig. 7). The updraft observed in the streamlines as well as the increase in turbulence intensity can be the cause of the dispersion of resuspended particles from the floor to upper regions closer to the BZ.

Similarly, a wake flow field with a triangular shape was formed with



**Fig. 8.** Experimental and predicted CFD values of the airflow field velocities measured at a height of: a)  $z = 0.3$  m, b)  $z = 0.8$  m, c)  $z = 1.2$  m and d)  $z = 1.5$  m for the entire prayer cycle.

peak velocities of 1 m/s. However, it trailed behind the front part of the manikin body. The velocity vectors between [6.5 s - 8 s] (See Fig. 9), showed that the flow was moving upwards in the region between the manikin's current and initial kneeling positions, which can cause particle dispersion. According to Fig. 8 during I2, the measured and predicted velocities increased gradually at the different heights as the manikin approached the measurement locations seen in Fig. 5(a). The predicted/measured velocities reach maximum values of 0.18 m/s ( $0.19 \pm 0.02$  m/s), 0.2 m/s ( $0.21 \pm 0.02$  m/s), 0.22 m/s ( $0.21 \pm 0.02$  m/s) and 0.22 m/s ( $0.21 \pm 0.02$  m/s) for heights of

$z = 0.3$  m, 0.8 m, 1.2 m and 1.5 m respectively. Good agreement was found between experimental and predicted values with a maximum relative error of 13.3% obtained at  $z = 1.2$  m at 9.5 s. These peak values were similar to the ones obtained during I1 due to similar manikin velocity. It can also be seen in Fig. 8 during I2 that, after the manikin crossed the measuring locations, the velocities at all heights decreased after the peak, to reach the background velocities once more.

When the manikin reached the initial prayer cycle position, the motion stopped and the prayer cycle ended at  $t = 12$  s. According to Fig. 9 at 12 s, no pressure difference or airflow circulation existed

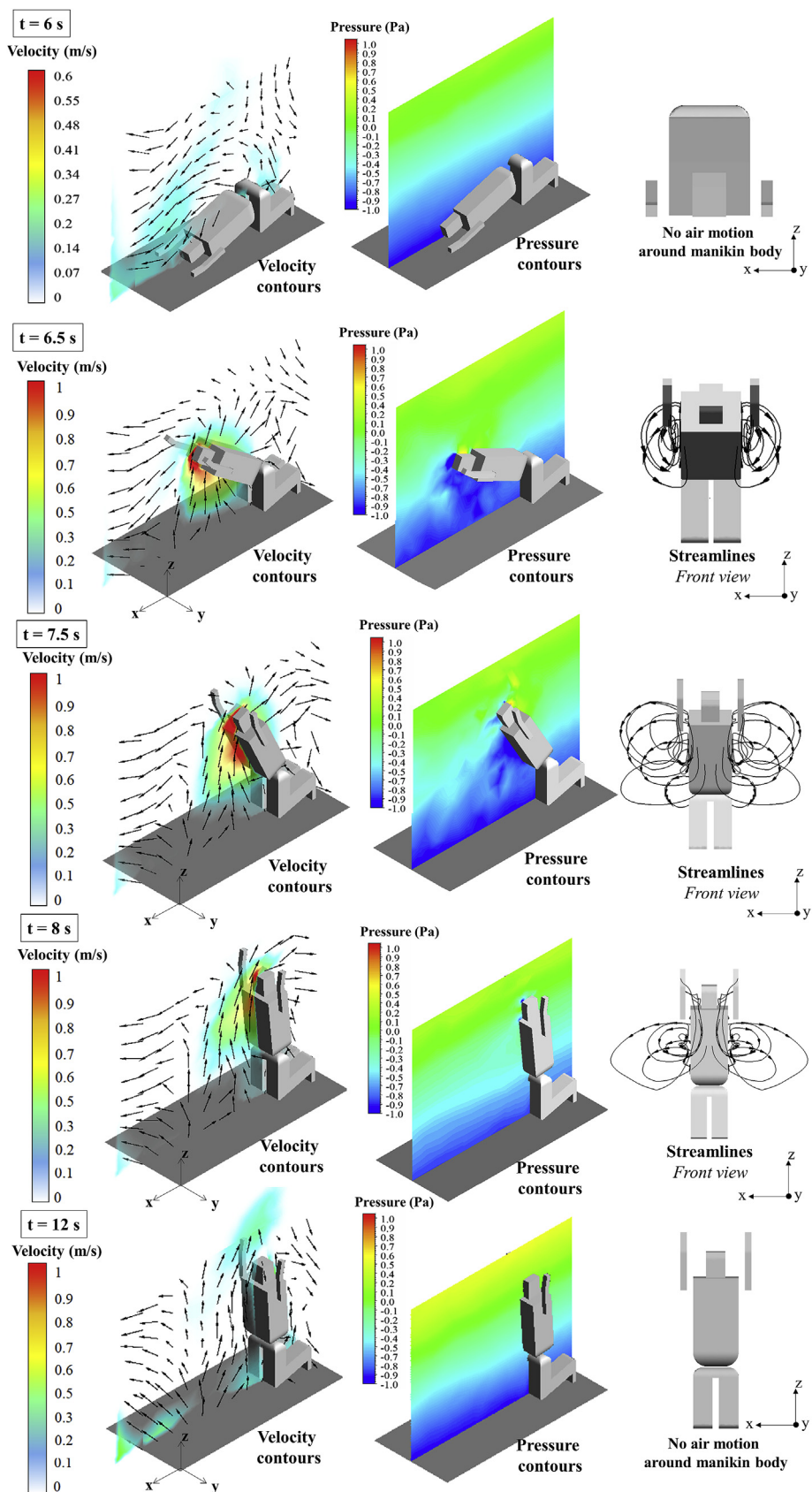


Fig. 9. Illustration of velocity contours, pressure contours in the  $y$  center plane ( $y = 1.7\text{ m}$ ) and 3-D velocity streamlines between  $t = [6\text{ s}–12\text{ s}]$ .

between the front and back. Moreover, turbulence intensities at the head and trunk dropped to 12% (see Fig. 7,  $t = 12$  s). As for the wake, its velocity diminished to 0.2 m/s and according to the velocity vectors; the wake was transported above the manikin head (see Fig. 9 at  $t = 12$  s). Note that the thermal plume started to form again due to buoyancy effects. However, it remained close to the body since it didn't have the time to rise above the manikin. According to Fig. 8, the predicted and measured velocities at all heights drop to the background velocities. This was due to the dissipation of the wake flow as well as the 40% decrease in turbulence intensities around the manikin.

### 3.2. Effect of manikin motion on particle dispersion and IAQ

#### 3.2.1. Breathable air quality and particles' behavior

Due to the wake flow field, generated particles from the floor ( $d_p$  of  $1 \mu\text{m}$  and  $10 \mu\text{m}$ ) can re-disperse and reach the occupant BZ and deteriorate IAQ. The breathable air quality was assessed in the second part

of the prayer cycle once the person reached prostration (at  $t = 2$  s) until the end of the cycle (at  $t = 12$  s). The results of particle behavior and breathable air quality are illustrated in Figs. 10 and 11. Fig. 10 shows the values of  $IF_{BZ}$  as a function of time and hence position for particle diameters of  $1 \mu\text{m}$  and  $10 \mu\text{m}$ . Figs. 11 and 12 show the particle trajectories within  $-0.2$  m to  $0.2$  m laterally from the  $y = 1.7$  mid-plane of the body and the contours of concentration at the mid-plane. The particles are represented by spheres. The particles colored in red corresponded to the closest particles ( $y = 1.5$  m plane) while the lightest gray color corresponded to the furthest particles ( $y = 1.9$  m plane). The particle trajectories and concentrations are shown from  $t = 6$ – $12$  s for particle diameters of  $1 \mu\text{m}$  (Figs. 11) and  $10 \mu\text{m}$  (Fig. 12).

According to Fig. 10(b), the  $IF_{BZ}$  decreased gradually with time as the occupant shifts from the prostration to the kneeling position. This is expected since the occupant was moving away from the floor pollution source. However, the  $IF_{BZ}$  decreased at varying rates depending on the angular position of the manikin in the cycle. Based on the simulations of

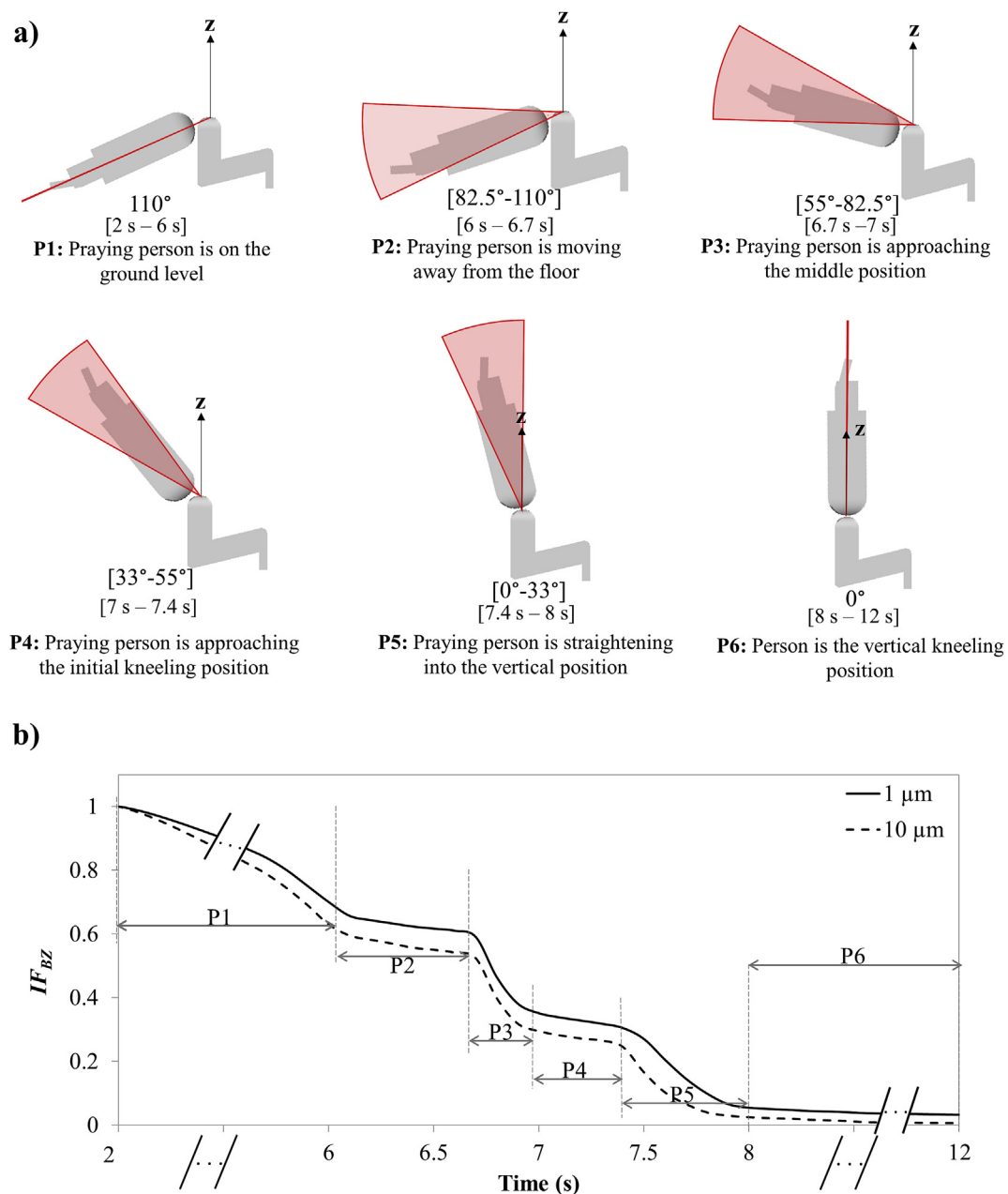


Fig. 10. Illustration of: a) the different phases of the manikin praying cycle P1 – P6, b) the  $IF_{BZ}$  variation with time for particle diameters of  $1 \mu\text{m}$  and  $10 \mu\text{m}$ .

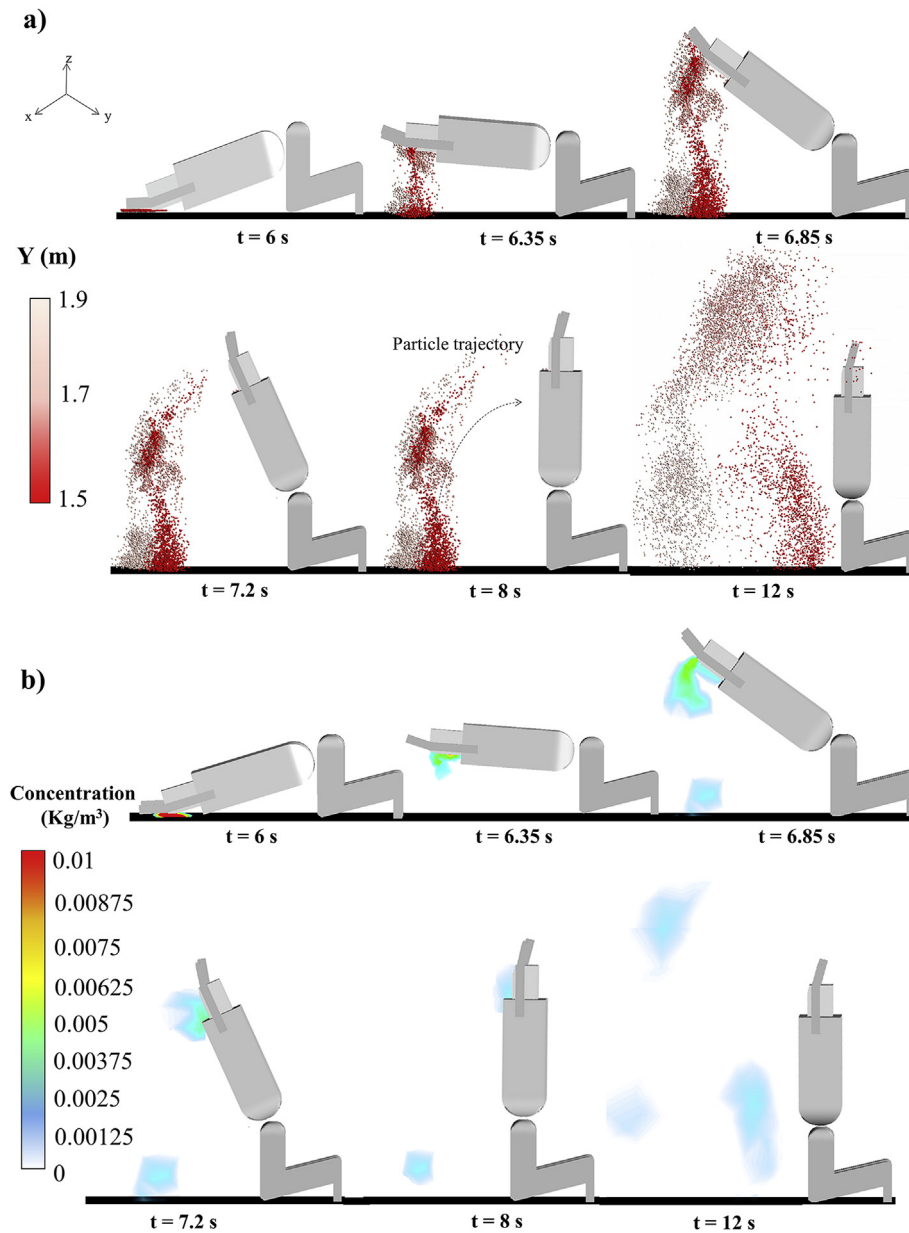


Fig. 11. Illustration of: a) particle dispersion caused by the praying manikin and b) DPM concentration contours from 6 s to 12 s, for  $1 \mu\text{m}$  particles.

the prostration cycle, six different phases were recognized. These phases from **P1** to **P6** can be seen in Fig. 10(a). Amongst these positions, the positions with the significant decrease rates: **P1**, **P3** and **P5** were discussed below.

During the first position **P1** from  $t = 2$  s–6 s, the  $IF_{BZ}$  had a value of 1 at  $t = 2$  s for both particle diameters showing that at the moment of resuspension, the person inhaled the maximum amount of particles from the floor. During **P1** between 2 s and 6 s, the  $IF_{BZ}$  started to decrease gradually by 35% and 41% for particle diameters of  $1 \mu\text{m}$  and  $10 \mu\text{m}$  respectively. In the absence of motion during **P1**, resuspended particles started to gradually deposit on the ground moving away from the BZ. This can be further seen in Figs. 11(b) and 12(b) which show the contours of DPM concentrations from  $t = 6$  s to  $t = 12$  s for  $1 \mu\text{m}$  and  $10 \mu\text{m}$  respectively.

When the occupant was in the third position **P3**, the  $IF_{BZ}$  decreased considerably by 40% and 44% for particle diameters of  $1 \mu\text{m}$  and  $10 \mu\text{m}$  respectively (See Fig. 10). During **P3**, the distance between the person and the floor becomes significant as seen in Figs. 11 and 12 at  $t = 6.85$  s. Additionally, the particles followed the same circular

trajectory as the wake flow propagating higher into the space. This meant that most of the particles that reached the BZ during **P2** started to move away from the BZ and further inside the wake mimicking its radial path. When the occupant reaches position **P5**, a faster decrease of 82% and 90% was noted for the  $IF_{BZ}$  for particle diameters of  $1 \mu\text{m}$  and  $10 \mu\text{m}$  respectively. During this time, the occupant was straightening into the vertical upright kneeling position. In this case, in order for particles to reach the BZ, they needed to be transported in the horizontal direction (see Fig. 11 at 8 s). However, it was shown that the particles' behavior was governed by the wake and according to the velocity in Fig. 9 (at 7.5 s and 8 s), the horizontal component that can transport the particles closer to the BZ was much smaller than the vertical component moving the particles higher up. Consequently, the amount of particles in the BZ decreased considerably during position **P5**.

It is noteworthy that similar  $IF_{BZ}$  trends and particle behaviors were noted for both  $1 \mu\text{m}$  and  $10 \mu\text{m}$  particles. However, the  $IF_{BZ}$  for  $1 \mu\text{m}$  was higher than the  $IF_{BZ}$  for  $10 \mu\text{m}$  from **P1** till **P6**. In addition, the decrease in  $IF_{BZ}$  during each position from **P1** to **P6** was more

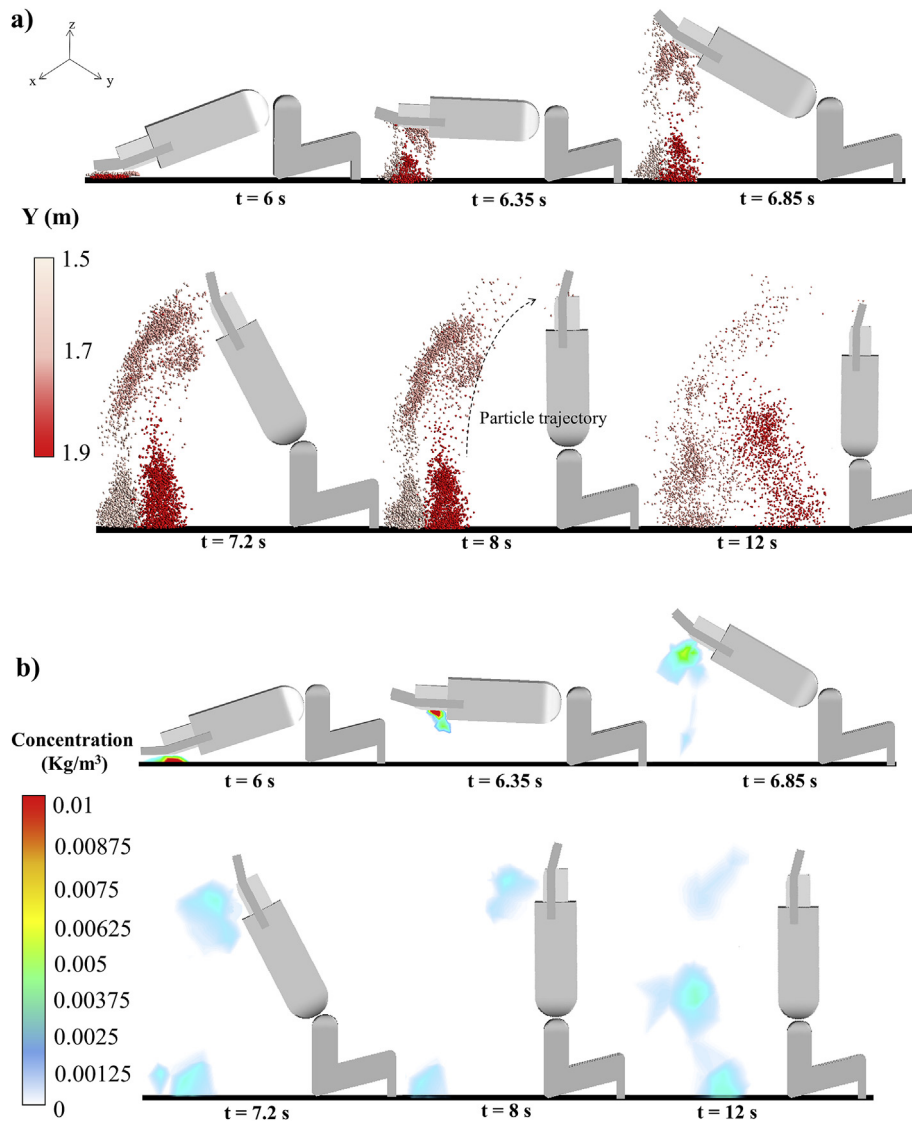


Fig. 12. Illustration of: a) particle dispersion caused by the praying manikin and b) DPM concentration contours from 6 s to 12 s, for 10 µm particles.

significant for 10 µm particles since larger particles were more affected by gravitational settling and could not reach the BZ at higher manikin positions. A larger amount of these particles were re-deposited on the floor, compared to 1 µm particles which are lighter and can disperse and reach the BZ more easily. As seen in Fig. 12(a), a larger amount of 10 µm particles was found near the floor compared to 1 µm particles. In addition, as seen in Fig. 11(a), a larger amount of 1 µm particles can be found at the BZ compared to 10 µm particles.

In conclusion, the prayer cycle performed by praying people inside prayer rooms or mosques, where the floor is a pollution source, constitutes a health risk and can deteriorate breathable air quality. The impact of the person with the ground during prostration resuspended particles which were inhaled, due to the close proximity of the BZ to the floor. Moreover, the wake flow generated by the rotation of the praying person generated significant airflow speeds and turbulence which can transport particles from lower levels near the floor to higher levels. It was also seen that the smaller the particle size, the higher the contamination risk since smaller lighter particles are more easily transported into the wake and hence the BZ as the person shifts from prostration to the kneeling position. Consequently, in mosque and multi-faith spaces involving occupant praying motion, it is important to minimize the resuspension rates from the floor by efficient techniques. These techniques include the right choice of the HVAC system, adopting

efficient cleaning techniques as well as choosing the right flooring material which would minimize particle detachment.

### 3.3. Limitations and future work

In this work, it is worthy to mention that the adopted particle injection method has certain limitations since the mass flow rate of injected particles highly affects dispersion pattern. Adopted method assumes that the injected mass flow rate is unaffected by the flow disturbance at the floor level. Therefore, a resuspension model should be developed in future work to compute the exact mass flow rate of particles detached from the surface and hence dispersed due to the prayer cycle.

In addition, the choice of air conditioning system in the multi-faith space can affect the macroclimate airflow field behavior and turbulence levels which could have a significant impact on particle dispersion. In this work, the space was conditioned with the conventional MV system. However, the choice of the HVAC system could constitute a parameter for future work. Moreover, the manikin rotation velocity depends on the age of praying people and can also constitute a variable parameter for future investigations. In this study, an average manikin rotation velocity of 0.9 rad/s was adopted to represent the average population.

#### 4. Conclusion

A 3-D CFD model of a praying space coupled with a dynamic mesh was developed to study the airflow field behavior of the Islamic prayer cycle and how that airflow field affected the dispersion of particles resuspended from the contaminated floor. It was shown that the rotation motion of the occupant during prayer generated a wake flow field that followed the body. The wake flow field was shown to generate significant airflow velocities reaching 1 m/s and turbulence intensity reaching 20%. Due to this wake, particles resuspended from the floor due to the impact of the person with the ground, follow the same radial trajectory as the wake. Therefore, particles can be transported from the floor to high levels of 1.4 m in the space. When the person is in the prostration position, the breathable air quality is deteriorated for all particles sizes due the proximity of the person to the ground. Additionally, it was found that smaller particles constitute a higher risk of contamination to the praying person. In fact, they can be easily transported by the wake to higher levels and contaminate the BZ, compared to heavier particles which remain closer to the floor. Therefore, in praying spaces, it is important to consider flooring types, ventilation system and cleaning strategies as design parameters to minimize the contamination risk of praying occupants.

#### Acknowledgments

The authors would like to acknowledge the financial support of the University Research Board of the American University of Beirut grant award. In addition, the American University of Beirut PhD scholarship to Ms. Al Assaad is highly acknowledged.

#### References

- [1] P. Pluschke, *Indoor Air Pollution, the Handbook of Environmental Chemistry*, Springer, 2018, <https://doi.org/10.1007/978-3-662-56065-5>.
- [2] Y.A. Horr, M. Arif, A. Kaushik, A. Mazroei, M. Katafygiotou, E. Elsarraj, Occupant productivity and office indoor environment quality: a review of the literature, *Build. Environ.* 105 (2016) 369–389, <https://doi.org/10.1016/j.buildenv.2016.06.001>.
- [3] C.-C. Jung, P.-C. Wu, C.-H. Tseng, H.-J. Su, Indoor air quality varies with ventilation types and working areas in hospitals, *Build. Environ.* 85 (2015) 190–195, <https://doi.org/10.1016/j.buildenv.2014.11.026>.
- [4] G. Adamkiewicz, *WHO Guidelines for Indoor Air Quality: Selected Pollutants*, World Health Organization, Geneva, 2010.
- [5] Environmental Topics, EPA, (2018) <https://www.epa.gov/environmental-topics>, Accessed date: 14 November 2018.
- [6] J. Qian, J. Peccia, A.R. Ferro, Walking-induced particle resuspension in indoor environments, *Atmos. Environ.* 89 (2014) 464–481, <https://doi.org/10.1016/j.atmosenv.2014.02.035>.
- [7] K. Belanger, Symptoms of wheeze and persistent cough in the first year of life: associations with indoor allergens, air contaminants, and maternal history of asthma, *Am. J. Epidemiol.* 158 (2003) 195–202, <https://doi.org/10.1093/aje/kwg148>.
- [8] T. Mimura, T. Ichinose, S. Yamagami, H. Fujishima, Y. Kamei, M. Goto, et al., Airborne particulate matter (PM<sub>2.5</sub>) and the prevalence of allergic conjunctivitis in Japan, *Sci. Total Environ.* 487 (2014) 493–499, <https://doi.org/10.1016/j.scitotenv.2014.04.057>.
- [9] Y. Kim, A. Gidwani, M. Sippola, C.W. Sohn, Source Term Model for Fine Particle Resuspension from Indoor Surfaces, (2008), <https://doi.org/10.21236/ada478661>.
- [10] A. Ibrahim, P. Dunn, R. Brach, Microparticle detachment from surfaces exposed to turbulent air flow: controlled experiments and modeling, *J. Aerosol Sci.* 34 (2003) 765–782, [https://doi.org/10.1016/s0021-8502\(03\)00031-4](https://doi.org/10.1016/s0021-8502(03)00031-4).
- [11] C. Habchi, K. Ghali, N. Ghaddar, Coupling CFD and analytical modeling for investigation of monolayer particle resuspension by transient flows, *Build. Environ.* 105 (2016) 1–12, <https://doi.org/10.1016/j.buildenv.2016.05.025>.
- [12] H.K. Hyytiäinen, B. Jayaprakash, P.V. Kirjavainen, S.E. Saari, R. Holopainen, J. Keskinen, et al., Crawling-induced floor dust resuspension affects the microbiota of the infant breathing zone, *Microbiome* 6 (2018), <https://doi.org/10.1186/s40168-018-0405-8>.
- [13] Y. Tao, K. Inthavong, J. Tu, Dynamic meshing modelling for particle resuspension caused by swinging manikin motion, *Build. Environ.* 123 (2017) 529–542, <https://doi.org/10.1016/j.buildenv.2017.07.026>.
- [14] H. Brohus, K.D. Balling, D. Jeppesen, Influence of movements on contaminant transport in an operating room, *Indoor Air* 16 (2006) 356–372, <https://doi.org/10.1111/j.1600-0668.2006.00454.x>.
- [15] G. Cao, H. Awbi, R. Yao, Y. Fan, K. Sirén, R. Kosonen, et al., A review of the performance of different ventilation and airflow distribution systems in buildings, *Build. Environ.* 73 (2014) 171–186, <https://doi.org/10.1016/j.buildenv.2013.12.009>.
- [16] I. Budaiwi, A. Abdou, HVAC system operational strategies for reduced energy consumption in buildings with intermittent occupancy: the case of mosques, *Energy Convers. Manag.* 73 (2013) 37–50, <https://doi.org/10.1016/j.enconman.2013.04.008>.
- [17] M. Kraljević, A. Simone, B.W. Olesen, Air distribution and ventilation effectiveness in an occupied room heated by warm air, *Energy Build.* 55 (2012) 94–101, <https://doi.org/10.1016/j.enbuild.2012.08.015>.
- [18] D. Müller, C. Kandzia, R. Kosonen, A.K. Melikov, P.V. Nielsen, *Mixing Ventilation Guide on mixing air distribution design*, 19 (2013) REHVA Guidebook No.
- [19] <https://www.pbslearningmedssia.org/resource/islam08.socst.world.glob.muslimpray/muslim-prayer>, Accessed December 20, 2018..
- [20] <http://www.sunna.info/prayer/TheBasicsoftheMuslimsPrayer.php>.
- [21] A. Makhoul, K. Ghali, N. Ghaddar, W. Chakroun, Investigation of particle transport in offices equipped with ceiling-mounted personalized ventilators, *Build. Environ.* 63 (2013) 97–107, <https://doi.org/10.1016/j.buildenv.2013.02.004>.
- [22] D. Coakley, P. Rafferty, M. Keane, Corrigendum to “A review of methods to match building energy simulation models to measured data”, *Renew. Sustain. Energy Rev.* 37 (2014) 123–141, <https://doi.org/10.1016/j.rser.2014.11.046> *Renewable and Sustainable Energy Reviews*. 43 (2015) 1467.
- [23] Engineering Simulation Software News and Insights, [https://www.ansys.com/blog/tag/ANSYS\\_HFSS\\_3D..](https://www.ansys.com/blog/tag/ANSYS_HFSS_3D..)
- [24] Y. Wu, N. Gao, The dynamics of the body motion induced wake flow and its effects on the contaminant dispersion, *Build. Environ.* 82 (2014) 63–74, <https://doi.org/10.1016/j.buildenv.2014.08.003>.
- [25] T.-T. Chow, J. Wang, Dynamic simulation on impact of surgeon bending movement on bacteria-carrying particles distribution in operating theatre, *Build. Environ.* 57 (2012) 68–80, <https://doi.org/10.1016/j.buildenv.2012.04.010>.
- [26] Z. Han, W. Weng, Q. Huang, Numerical and experimental investigation on the dynamic airflow of human movement in a full-scale cabin, *HVAC R Res.* 20 (2014) 444–457, <https://doi.org/10.1080/10789669.2014.882677>.
- [27] D.A. Assaad, K. Ghali, N. Ghaddar, Effectiveness of intermittent personalized ventilation assisting a chilled ceiling for enhanced thermal comfort and acceptable indoor air quality, *Build. Environ.* 144 (2018) 9–22, <https://doi.org/10.1016/j.buildenv.2018.08.005>.
- [28] S. Liu, A. Novoselac, Lagrangian particle modeling in the indoor environment: a comparison of RANS and LES turbulence methods (RP-1512), *HVAC R Res.* 20 (2014) 480–495, <https://doi.org/10.1080/10789669.2014.884380>.
- [29] B. Blocken, LES over RANS in building simulation for outdoor and indoor applications: a foregone conclusion? *Build. Simul.* 11 (2018) 821–870, <https://doi.org/10.1007/s12273-018-0459-3>.
- [30] M. Lateb, C. Masson, T. Stathopoulos, C. Bédard, Simulation of near-field dispersion of pollutants using detached-eddy simulation, *Comput. Fluids* 100 (2014) 308–320, <https://doi.org/10.1016/j.compfluid.2014.05.024>.
- [31] H.A. Olvera, A.R. Choudhuri, W.-W. Li, Effects of plume buoyancy and momentum on the near-wake flow structure and dispersion behind an idealized building, *J. Wind Eng. Ind. Aerod.* 96 (2008) 209–228, <https://doi.org/10.1016/j.jweia.2007.04.004>.
- [32] Y. Tominaga, A. Mochida, R. Yoshie, H. Kataoka, T. Nozu, M. Yoshikawa, et al., AIJ guidelines for practical applications of CFD to pedestrian wind environment around buildings, *J. Wind Eng. Ind. Aerod.* 96 (2008) 1749–1761, <https://doi.org/10.1016/j.jweia.2008.02.058>.
- [33] D.A. Assaad, K. Ghali, N. Ghaddar, C. Habchi, Mixing ventilation coupled with personalized sinusoidal ventilation: optimal frequency and flow rate for acceptable air quality, *Energy Build.* 154 (2017) 569–580, <https://doi.org/10.1016/j.enbuild.2017.08.090>.
- [34] D.A. Assaad, C. Habchi, K. Ghali, N. Ghaddar, Effectiveness of intermittent personalized ventilation in protecting occupant from indoor particles, *Build. Environ.* 128 (2018) 22–32, <https://doi.org/10.1016/j.buildenv.2017.11.027>.
- [35] C. Habchi, K. Ghali, N. Ghaddar, W. Chakroun, S. Alotaibi, Ceiling personalized ventilation combined with desk fans for reduced direct and indirect cross-contamination and efficient use of office space, *Energy Convers. Manag.* 111 (2016) 158–173, <https://doi.org/10.1016/j.enconman.2015.12.067>.
- [36] C. Habchi, K. Ghali, N. Ghaddar, A. Shihadeh, Chair fan-enhanced displacement ventilation for high IAQ: effects on particle inhalation and stratification height, *Build. Environ.* 84 (2015) 68–79, <https://doi.org/10.1016/j.buildenv.2014.10.019>.
- [37] H.E. Khalifa, B. Elhadidi, Particle levitation due to a uniformly descending flat object, *Aerosol Sci. Technol.* 41 (2007) 33–42, <https://doi.org/10.1080/02786820601064857>.
- [38] X. Zhang, G. Ahmadi, J. Qian, A. Ferro, Particle detachment, resuspension and transport due to human walking in indoor environments, *J. Adhes. Sci. Technol.* 22 (2008) 591–621, <https://doi.org/10.1163/156856108x305624>.
- [39] Y. Tian, K. Sul, J. Qian, S. Mondal, A.R. Ferro, A comparative study of walking-induced dust resuspension using a consistent test mechanism, *Indoor Air* 24 (2014) 592–603, <https://doi.org/10.1111/ina.12107>.
- [40] A.Q. Ahmed, S. Gao, Numerical investigation of height impact of local exhaust combined with an office work station on energy saving and indoor environment, *Build. Environ.* 122 (2017) 194–205, <https://doi.org/10.1016/j.buildenv.2017.06.011>.
- [41] S. Keshavarz, M. Salmanzadeh, G. Ahmadi, Computational modeling of time resolved exposure level analysis of a heated breathing manikin with rotation in a room, *J. Aerosol Sci.* 103 (2017) 117–131, <https://doi.org/10.1016/j.jaerosci.2016.09.005>.
- [42] S. Alotaibi, W. Chakroun, C. Habchi, K. Ghali, N. Ghaddar, Effectiveness of contaminant confinement in office spaces equipped with ceiling personalized

- ventilation system, *Build. Simul.* 11 (2018) 773–786, <https://doi.org/10.1007/s12273-018-0437-9>.
- [43] B. Zhao, Y. Zhang, X. Li, X. Yang, D. Huang, Comparison of indoor aerosol particle concentration and deposition in different ventilated rooms by numerical method, *Build. Environ.* 39 (2004) 1–8, <https://doi.org/10.1016/j.buildenv.2003.08.002>.
- [44] B. Zhao, P. Guan, Modeling particle dispersion in personalized ventilated room, *Build. Environ.* 42 (2007) 1099–1109, <https://doi.org/10.1016/j.buildenv.2005.11.009>.
- [45] B. Zhao, C. Chen, Z. Tan, Modeling of ultrafine particle dispersion in indoor environments with an improved drift flux model, *J. Aerosol Sci.* 40 (2009) 29–43, <https://doi.org/10.1016/j.jaerosci.2008.09.001>.
- [46] M. Kazzaz, C. Habchi, K. Ghali, N. Ghaddar, S. Alotaibi, W. Chakroun, Micro-particle indoor resuspension under periodic airflows: a numerical-analytical study and experimentations, *Build. Environ.* 123 (2017) 299–314, <https://doi.org/10.1016/j.buildenv.2017.07.011>.
- [47] A.A. Rostami, S. Agyemang, Y.B. Pithawalla, A distributed computational model for estimating room air level of constituents due to aerosol emission from e-vapor product use, *Food Chem. Toxicol.* 116 (2018) 114–128, <https://doi.org/10.1016/j.fct.2018.04.020>.
- [48] H. Yu, K. Mui, L. Wong, Numerical simulation of bioaerosol particle exposure assessment in office environment from MVAC systems, *J. Comput. Multiph. Flows* 10 (2017) 59–71, <https://doi.org/10.1177/1757482x17746919>.
- [49] Y. Zhou, Y. Deng, P. Wu, S.-J. Cao, The effects of ventilation and floor heating systems on the dispersion and deposition of fine particles in an enclosed environment, *Build. Environ.* 125 (2017) 192–205, <https://doi.org/10.1016/j.buildenv.2017.08.049>.
- [50] I. Goldasteh, Y. Tian, G. Ahmadi, A.R. Ferro, Human induced flow field and resultant particle resuspension and transport during gait cycle, *Build. Environ.* 77 (2014) 101–109, <https://doi.org/10.1016/j.buildenv.2014.03.016>.
- [51] B.A. Edge, E.G. Paterson, G.S. Settles, Computational study of the wake and contaminant transport of a walking human, *J. Fluid Eng.* 127 (2005) 967, <https://doi.org/10.1115/1.2013291>.